e-ISSN 2320 –7876 www.ijfans.org
Vol.11, Iss.9, Dec 2022

Research Paper

SYNTHESIS AND CHARACTERISATION OF NANOMATERIAL

ESWARI.G
Research Scholar
M.Phil Physics
Bharath Institute Of Higher Education And Research
Mail Id : mahalingameswari@gmail.com
Guide Name: **Dr.K.THIYAGARAJAN**
Head of the Department, Department Of Physics
Bharath Institute Of Higher Education And Research

Address for Correspondence

ESWARI.G
Research Scholar
M.Phil Physics
Bharath Institute Of Higher Education And Research
Mail Id : mahalingameswari@gmail.com
Guide Name: **Dr.K.THIYAGARAJAN**
Head of the Department, Department Of Physics
Bharath Institute Of Higher Education And Research

ABSTRACT

Because metal oxides are a varied and interesting class of material with characteristics ranging from metals to semiconductors and insulators, major advancement in the area of material science is largely reliant on their development. Perovskite crystal formations are a kind of oxide material with unique functional characteristics that are needed for further technological advancement. Because synthesis of single-phase BiFeO3 (BFO) material is challenging owing to the high volatility of Bi ions, we have utilised a variety of preparation methods to achieve pure phase multiferroic material in this thesis. Synthesis and characterisation of pure and doped bismuth ferrite thin films and polycrystalline bulk material are the primary emphasis. In the current study, pure and doped BFO bulk and thin film nanomaterial were produced to evaluate the suitability of doping components for the improvement of different physical characteristics. As a function of composition, sintering/annealing temperature, frequency, and magnetic field, the structural/microstructural, dielectric, magnetic, and optical characteristics of nanomaterial are investigated. The purpose of this thesis is to investigate structural, microstructural, electrical, and multiferroic characteristics, as well

as their relationships. However, owing to a shortage of instrumentation, the magnetoelectric (ME) measurement could not be performed. The characteristics of the material examined in detail are summarised. The surface morphology of the samples revealed the development of nano-scale samples that were produced by chemical means. The EDX spectra of the produced material show that all samples are free of foreign elements except for the suggested elements, and the samples have anticipated stoichiometry. The samples' dielectric characterisation was carried out across a broad frequency range. All of the changed samples' M-H loops exhibited antiferromagnetics/weak ferromagnetics behaviour at ambient temperature. material can be ascribed to the presence of magnetism in the samples, which eventually move towards the field direction, giving rise to weak ferromagnetism.

Introduction

Recently, functional oxide material have become important research area in our scientific community because of their attractive physical phenomena along with wide range of applications. These oxide material have involved much courtesy due to their broad range of functional properties viz. ferroelectric [1-3], thermo- electric [4], pyroelectric [5], dielectric [6,7], optical [8], magnetic [9, 10], superconducting properties [11, 12]. Due to these interesting physical properties, oxide material have a great significant interest to design new functional devices such as random access memories [13], tunable microwave devices [14], super- capacitors [15], displays [16], transducer devices [17], sensors [18, 19], actuators [19], wireless communications [20] and spintronic devices [21]. The electronic and magnetic proerties of these material are crucial part of modern physics for the development of new generation smart functional devices. The ferromagnetics/ magnetic/electric field due to the presence of magnetic domains and the electric dipole. Therefore, these oxide material show hysteresis loop either in the presence of external magnetic orelectric field [22]. Besides the ferroelectricity and ferromagnetism, the material have two other ferroic properties for example, ferroelastic and ferrotorroidic in same phase [23]. The ferroelasticity exhibits a spontaneous stretching without an external strain and ferrotoroidicity shows a spontaneous growth of magnetic vortices [24, 25]. The ferroic orders are unique functional properties required for continuous technological growth and essential to design the ferroelectric and magneto-resistive random access memory devices [26However, there are very few material that exhibit magnetoelectric properties strongly dependent on specific conditions of the synthesis process. The functionality of multiferroic material can be tuned with the change of electric field,

magnetic field, stress, strain and temperature. In the current research, multiferroic material have attracted tremendous interest due its potential applications. The various nanostructures for examples nanowires, nanorods, nano-sheets, nano-flowers, nano-tubes etc with their unique properties have been fabricated for device applications.

Basics of ferroelectric material

The first discovered ferroelectric material is Rochelle salt by Valasek in 1920 [42]. So far many ferroectric material (shown in table 1.1) have been synthesised.The microscopic mechanism and origins of ferroelectricity of functional material are enormous. The ferroelectricity arises in the crystal due to structural distortion caused by the off-centred shift of the small cations which produce permanent dipole moment. Essentially nonlinear dielectrics material exhibit the ferroelectric properties and show spontaneous electric polarization by external electric field. In other words, the ferroelectric material transformed from centrosymmetric phase to non- centrosymmetric phase. The crystalline material have different electrical polar behavior depending on the point group symmetry.

Magnetism requires the broken temporal reverse symmetry, but the spatial inverse symmetry remains invariant, according to crystallographic point group symmetry. Ferroelectrics, on the other hand, need a broken spatial inverse symmetry while maintaining invariant temporal reverse symmetry. Crystalline material contain 14 Bravais lattices in three-dimensional space, according to symmetry operations. Furthermore, when using mirror planes with symmetry operations such as the centre of symmetry, rotational axes (1, 2, 3, 4 and 6 fold), and inversion axes (1, 2, 3, 4 and 6 fold) on atomic unit cells, 32 potential point groups emerge. However, only 11 of the 32 point groups have a centre of symmetry with non-polar (polarisation) characteristics, whereas 21 lack symmetry and exhibit polar behaviour [43]. In the flow chart given in figure 1.1, the detailed point group symmetry has been described and effectively illustrated. Schmidt highlighted the need of tight symmetry requirements for the presence of ferroic characteristics. Depending on the mobility () of electrons inside the lattice, crystalline material exhibit various electrical/electronic characteristics such as conductivity, band gap, resistivity, carrier concentrations, current density, magnetoresistance, and so on. In terms of conductivity, crystalline material are classified into three categories: conductors, semiconductors, and insulators. Insulators are an unique kind of material having dielectric characteristics because the electrons are firmly bonded inside the crystal.

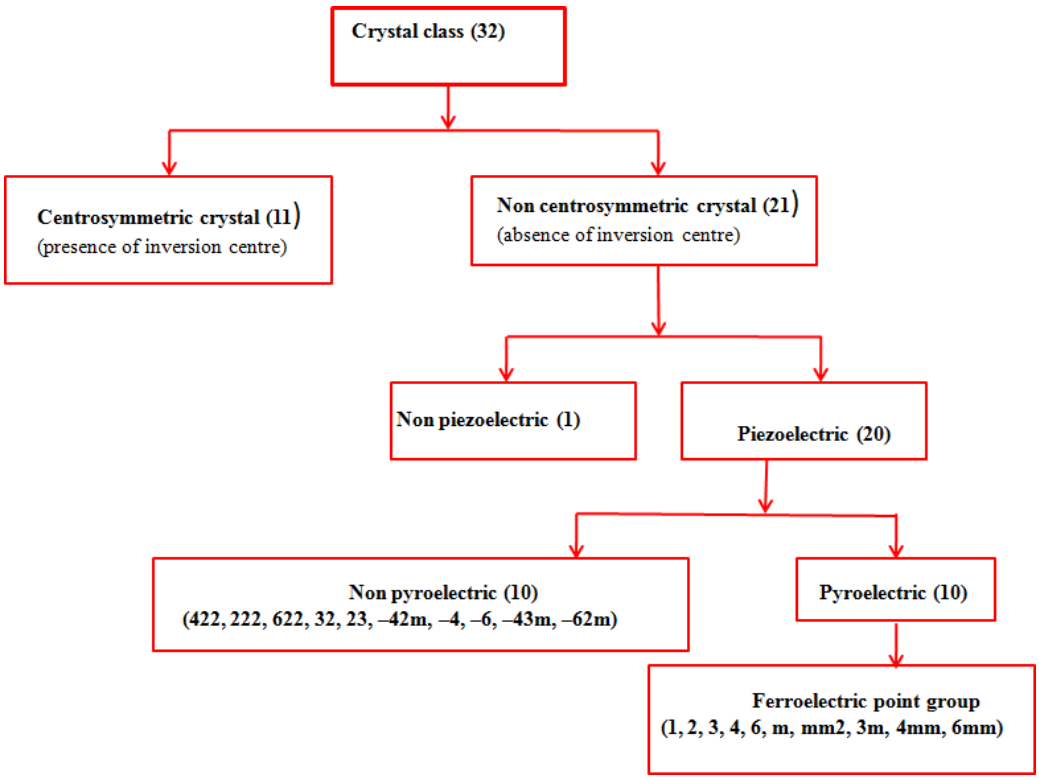

Figure 1.1: Ferroelectricity classified of on the basis of symmetry consideration

The insulator (dielectric) material are further classified into the subclasses depends on how the polarization varies with the external conditions such as (electric field, strain, stress and temperature). By applying strain the material generate an electric field (voltage) is known as piezoelectric material. The lead zirconate titanate ($PbZrTiO_3$) and barium titanate ($BaTiO_3$) are well known piezoelectric material. The barium titanate and lead zirconate titanate are soft and hard piezoelectric material which depend on the mobility as well as the polarization and depolarization behavior of the dipoles. The soft piezoelectric material generally are used in vibration detectors, ultrasonic transmitters, receivers and electro-acoustic applications due to its low schism setback arena strength. The hard piezoelectric material are mostly used in high-power acoustic application.

Basic of magnetic material

The notion of magnetism is a well-known phenomenon that results from the mobility of an electron

in an orbital or its spin motion, which results in magnetic characteristics. The magnetic characteristics of oxide material are determined by the properties of individual ions or atoms in a magnetic field. The magnetic characteristics of these atoms or ions in three-dimensional space are similarly linked to and changed by their electronic arrangement. Material' magnetic characteristics may be divided into five groups based on their microscopic magnetic susceptibility and dipole moment orientation. The magnetic characteristics of material are classified as diamagnetic, paramagnetic, ferromagnetics, antiferromagnetics, and ferrimagnetic based on how they behave under a magnetic field supplied externally. Magnetic material are divided into five groups based on their microscopic magnetic susceptibility and dipole moment orientation. Diamagnetic, paramagnetic, ferromagnetics, antiferromagnetics, and ferrimagnetic are the five most prevalent kinds of magnetic material. The magnetism arises due to spontaneous alignment of magnetic dipole moment or interaction among these magnetic moments resulting material show magnetic behaviour. The phenomena of ferromagnetism required partially field d orbital and breaking of the time reversal symmetry.

Diamagnetic material

When a magnetic field termed diamagnetic material is applied, the atom has moment. When a material is subjected to an applied field (H), the spinning electrons in the atomic orbital move in such a manner that they oppose the magnetic field, resulting in a magnetization (M) that is the polar opposite of the applied field. Diamagnetism is the name for this phenomenon.

1.3.2 Paramagnetic material There are many paramagnetic theories, one of which is the Langevin model, which explains the characteristics of this kind of material. The non-interacting localised electrons are despised by the paramagnetic material, which says that each atom has a field. The relationship C 1.3.3 Ferromagnetics material describes the temperature dependence of paramagnetic susceptibility. Ferromagnetism classical theory. The parallel alignment of magnetic moments is described by the Heisenberg model of ferromagnetism in among adjacent moments. Magnetic domains, or areas, are thought to exist inside the material, according to Weiss. When ferromagnetics material are heated, thermal decrease, resulting in a reduction in saturation magnetization.

e-ISSN 2320 –7876 www.ijfans.org
Vol.11, Iss.9, Dec 2022

Research Paper

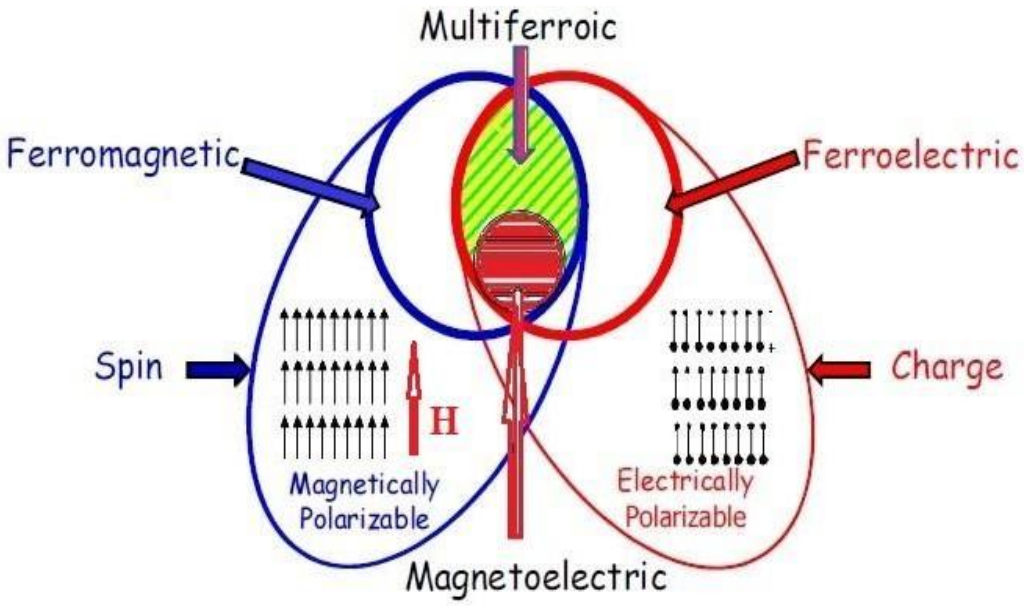

Figure 1.1 The coupling phenomenon of magnetic and electrical properties is a more general defined as magnetoelectric coupling [33].

Magnetic Properties of $BiFeO_3$

The single phase $BiFeO_3$ material possess G-type antiferromagnetics ordering where each Fe^{3+} ions is surrounded by six antiparallels nearest neighbour spins. The hard X-ray magnetic scattering gives the information about magnetic domains structure formed at the surface of $BiFeO_3$ single crystal. The rotation of the magnetization of all magnetic domains are clearly determined by diffraction of circularly polarized light [103]. The magnetic properties of BFO material strongly depend upon the O-vacancies. Afzal et al. has reported that BFO material annealed in air and oxygen, confirms the effect of O-vacancies on magnetic properties. The values of magnetization has been found to be 0.199 emu/g and 0.077 annealed at 450 ^{0}C and 650 ^{0}C in air whereas the value of magnetization increases and observed to be 1.2 emu/g and 0.089 emu/g annealedat 450 ^{0}C and 650 ^{0}C in oxygen atmosphere, respectively [104]. Zhou et al. [105] reported that $BiFeO_3$ nanorods prepared by hydrothermal technique and annealed under magnetic field suppress the modulated spin structure and enhanced the magnetization.

The single section BFO material own ferroelectric ordering at high Curie temperature (TC) ~ 1100

okay. A these days stated spontaneous polarization in BFO unmarried crystal is ~6.1 μC/cm2 along the (111) course at very low temperature 77 okay [106]. Palkar et al. [107] have mentioned saturation polarization (ps) 2.2 μC/cm2, remnant polarization (Pr) zero.83 μC/cm2 in BFO skinny films deposited on various substrates Pt/TiO2/SiO2/Si. Yun et al. [108] used the equal substrate and method as Palkar but lower oxygen strain (zero.01- 0.1Torr) at some stage in deposition and received desirable ferroelectric homes, excessive remanent polarization (2Pr) ~seventy one.3 μC/cm2 and coercive discipline (2Ec) ~one hundred twenty five kV/cm. Wang et al. have organized epitaxial BFO skinny films on SrRuO3/STO (a hundred) substrates through PLD approach and found massive remanent polarization 2Pr ~120 μC/cm2 [109]. however, Li et al. [110] have organized BFO thin films on STO substrate and inspect the ferroelectric homes and determined spontaneous polarization is ~zero.061 C/m2.

Applications of Multiferroic Material

The ferroelectric are important class of material that can be used in advanced electronic applications like high-energy compactness capacitor, actuator and piezoelectrics transducer. Ferroelectric thin films are essentially used to design next generation‟s electronic chips and ferroelectric random access memories (FE- RAMs) device. The ferromagnetics material have wide applications in new technologies like power generators, magnetic motors, data-storage devices, quantum devices (SQUID) and magnetic sensing. However, magnetoelectric multiferroic material possess both ferroelectric and magnetic ordering and cross coupling which provides new potential application in modern devices. The magnetoelectric (ME) material have generally used in magnetic reading/writing and GMR commercial technology. The composite and single-phase multiferroic material can be used in oscillators. The multiferroic thin films have novel applications such as tunnel magnetoresistance (TMR) sensors. The TMR device consists of three layers which are ferromagnetics, multiferroic and ferromagnetics material. In such apparatus, the ferromagnetics layer works as a tunnel barrier and spin transport across it can be electrically tuned. However, additional configuration contains of two layers of antiferromagnetics material unglued by a thin tunnel barrier which is prepared of a multiferroic thin film.

EXPERIMENTAL AND CHARACTERIZATION TECHNIQUES

Different aspects for the experimental techniques used in the present work are briefly described in this chapter. Chemical route (Sol-gel) for the synthesis of $BiFeO_3$ nanoparticles has been discussed.

e-ISSN 2320 –7876 www.ijfans.org
Vol.11, Iss.9, Dec 2022

Afterwards, the characterization techniques like X-ray diffraction (XRD), Raman spectra method, Transmission electron microscopy (TEM), Vibrating sample magnetometer (VSM), Electron spin resonance (ESR), Spin quantum interference device (SQUID), UV-Vis diffuse reflectance (UV-Vis) and Fourier transform infrared spectroscopy (FTIR) techniques are presented.

X-RAY DIFFRACTION TECHNIQUE

X-ray diffraction (XRD) is very powerful tool which is extensively used for the phase identification of material. This is also used for the analysis of lattice parameters, crystallite size, and crystal structures etc. In 1895, it was discovered by Roentgen that X-rays are electromagnetic waves and the phenomenon of X-ray was discovered by Max von Laue in 1912 [118]. The wavelength of X-rays is comparable to that of lattice spacing, therefore it is used to obtain diffraction pattern of crystals. This is mostly used for the determination of crystal structure and d-spacing (spacing among the planes). Basic principle to determine the crystal structure is based on the interaction of X-ray photons with the matter which results in the coherent scattering of photons.

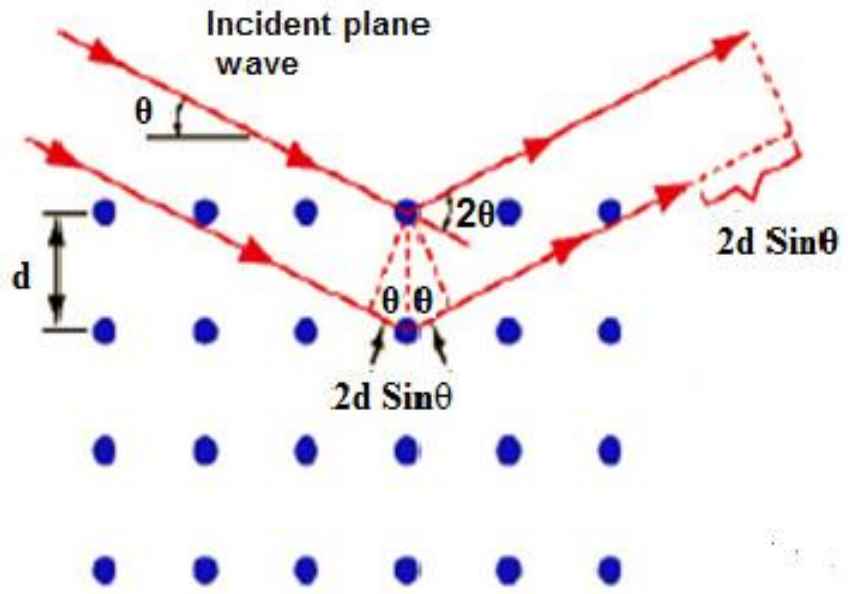

Figure 2.2: Systematic representation of Braggs diffraction for a set of lattice with d spacing.

e-ISSN 2320 –7876 www.ijfans.org
Vol.11, Iss.9, Dec 2022

X-ray diffraction works on the principle of constructive interference, when sample is exposed to electromagnetic radiations, x-rays (generated with the help of cathode ray tube) incident on the sample and interact with it. When the condition of Bragg's law satisfied ($n\lambda=2d\sin\theta$), constructive interference occurs. Bragg's law provides the relation of wavelength

with the angle of diffraction and lattice spacing of the sample. X-rays diffracted from the various planes are detected and counted. In the mean time the sample is rotate with angle 2θ to obtain all the possible direction of diffraction. After that these diffracted peaks are converted into d-spacingto identify the material. As each material has unique set of d-spacing, therefore identification of the material can easily be done by comparing the obtained set of d- spacing with the reference pattern. Systematic representation of Bragg's law is shown in **Figure 2.2.**

The powder diffractometer used to collect diffraction pattern is display in **Figure 2.3**. Firstly by heating the filament in cathode ray tube, x-rays are generated to produce electrons. These accelerated electrons collide with the target material and remove the electrons from the inner shell to generate an X-ray spectrum which is made up of various components, commonlyK_α and K_β. Further K_α is have two parts i.e $K_{\alpha1}$ and $K_{\alpha2}$, wave length of $K_{\alpha1}$ is short and its intensity is double compared to $K_{\alpha2}$. Mostly copper is used as a target material having CuK_α radiation = 1.5418Å. When X-rays interacts with the sample, constructive interference occurs when Bragg's law is satisfied. Whenever constructive interference occurs, a peak is obtained and is recorded by the detector. These signals were processed and converted into count rate.

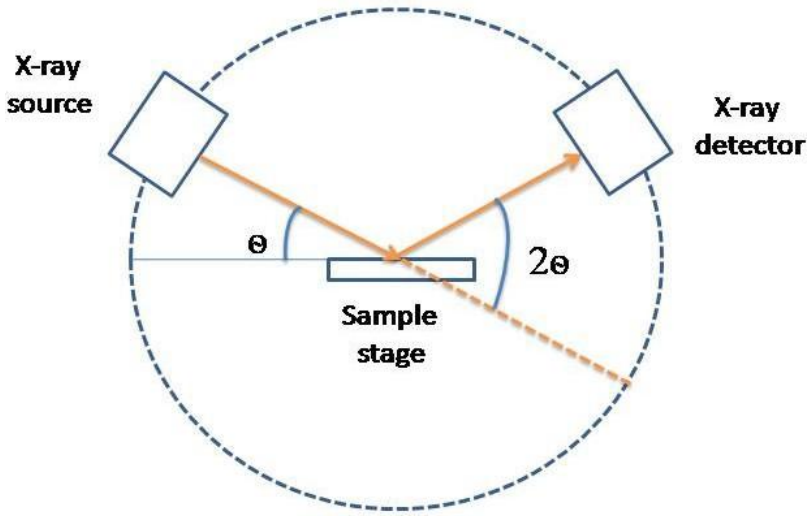

Figure 2.3: Schematic diagram shows X-ray diffractometer

The alignment of sample holder and detector is such that on rotating the sample through the angle θ, the detector which collects the X-rays rotates with an angle 2θ. Gonimeter is the instrument which is used to rotate the sample.

2.1.1 RAMAN SPECTROSCOPY

Raman scattering is very powerful tool which is used to measure the frequency of some vibrational modes in a molecule. Raman Effect is a light scattering phenomenon in which change in frequency occurs when the light is scattered. When the light irradiates over sample, it scattered and if the frequency of scattered light matches with the incident light, it is known as Rayleigh scattering or elastic scattering. However, if the frequency of scattered light lies below or above in comparison of frequency of incident light, the process is known as inelastic scattering and is termed as Raman Effect. In a molecule, changing in electronic, vibrational, and rotational energy level is responsible for the occurrence of Raman Effect. The Raman interaction results in two possible outcomes: is low than that of , it is termed as stokes while the light at higher than the frequency of incident light, it is referred as antistokes scattering.

e-ISSN 2320 –7876 www.ijfans.org
Vol.11, Iss.9, Dec 2022

Research Paper

Experimental details

Firstly, the precursor solution have been prepared by using analytic grade $Bi(NO_3)_3.5H_2O$ (99% Merck), $Fe(NO_3)_3.9H_2O$ (99% Merck) material weighing inappropriate amount and dissolve in ethylene glycol. The resultant precursor solution was stirred at 30 ^{0}C for 3 hours, thereafter a brownish transparent and clear solution was obtained. The few drops of nitric acid were added to get better clarity of the precursor solution. The 1 molar prepared sodium hydroxide (NaOH, Merck purity > 99%) solution was continuously added in precursor solution till the brownish colour precipitates were obtained at room temperature. This brownish colour precipitate was filtered and then washed by deionised distilled water and finally dried at 350 ^{0}C for 8 hours in well temperature controlled oven. The dried brownish powder was thoroughly ground and mixed for at least 5 hours in a mortar and pestle and then formed into pellets (15 mm diameter and a couple of mm thick) in hydraulic press machine. subsequently the pellets had been sintered at diverse temperatures from four hundred 0C to three hundred 0C for 10 hours. The gross crystal shape and segment purity of BFO cloth has been investigated by powder X-ray diffraction method. The diffraction facts become recorded inside the range of 20 to 30° at a step size of 0.02/min and scanning velocity of 10/min by means of the usage of a bruker D eight advanced x-ray diffractometer with CuKα (λ=1.5406Å) radiation at UGC-DAE Consortium for medical research, Indore. The floor topography and root imply square roughness of as sintered pellets had been observed by way of atomic force microscopy (virtual instrument Nanoscope–III a). The surface morphology of the gold (10 nm) lined sintered pallet has also been acquired the use of subject production scanning electron microscope (MIRA II LMH from TESCAN) with an attachment of strength dispersive spectroscopy (EDS) of x-rays at Inter-college Accelerator Centre (IUAC), New Delhi. The dielectric properties had been studied as a characteristic of frequency the usage of the Agilent network (E-4991A) with impedance analyser and LCR meter. Results and discussion

Crystalline phase and structural analysis

Figure 3.1, shows the representative x-ray diffraction (XRD) patterns of the BFO pellets

sintered at various temperatures of 400 ^{0}C, 500 ^{0}C, 600 ^{0}C and 300 ^{0}C.

The observed diffraction peaks/reflections such as (012), (104), (110), (202), (024), (116), (122), (300) and (208) have been well indexed with JCPDS (30- 5668) of rhombohedrally distorted crystal structure of $BiFeO_3$ with R3c space group. The few peaks/reflections belonging to the secondary phase-$Bi_2Fe_4O_9$ were also observed in the XRD pattern at lower sintering temperatures. It means that sintering the pellets reduces the formation of secondary phases. Though the intensity of the diffraction peaks gradually increases with increasing sintering temperature, nevertheless, full width at half maxima (FWHM) decreases. This indicates that the crystallite size is cumulative with the increasing sintering temperature. The regular crystallite size (D) of BFO polycrystalline pellets sintered at various temperatures is calculated using Scherrer formula

$$D = \frac{K\lambda}{\beta \cos \theta} \qquad (3.1)$$

Where K is continuous and its value for the sphere-shaped shape grains (0.9), λ is the x-ray wavelength, β is the full width at half maxima and θ is the Bragg angle. The average crystallite size of BFO pellets was found to increase from 20 nm to 36 nm as the sintering temperature increases from 400 ^{0}C to 300 ^{0}C.

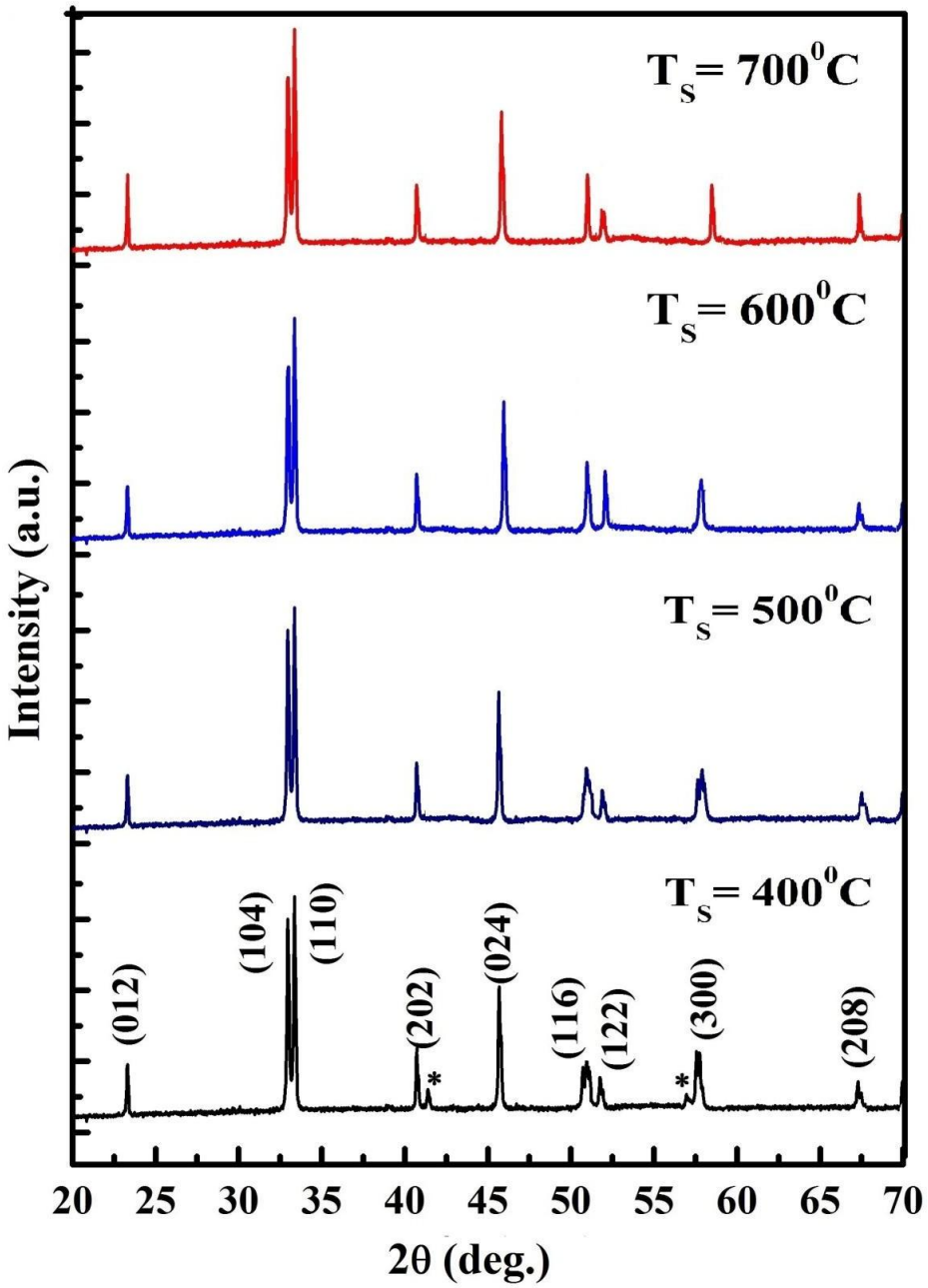

Figure 3.1 X- ray diffraction patterns of BFO sintered at 400 ^{0}C to 300 ^{0}C.

The lattice parameters of rhombohedral perovskite unit cell of BFO pellets sintered at numerous temperatures of 400 ^{0}C, 500 ^{0}C, 600 ^{0}C and 300 ^{0}C were also calculated from the XRD data and found to be **a= b**=5.5814 Å, **c**=13.832 Å; **a= b**=5.5819 Å, **c**=13.865 Å; **a= b**=5.5826 Å, **c**=13.852 Å; **a= b**=5.5836 Å, **c**=13.842
Å and **a= b**=5.5854 Å, **c**=13.836 Å respectively. It may be noticed here that the lattice constant a (=b) is increasing slightly and whereas c lattice parameter is decreasing marginally with increasing the sintering temperature from 400 ^{0}C to 300 ^{0}C. This indicates that there are no major changes in BFO crystal structure.

Williamson-Hall analysis

The lattice stress and more correct crystallite length of BFO pallets sintered at diverse temperatures have been decided with the aid of using Williamson-hall (W-H) method. it's miles empirical mathematical relation among the critical full widths at half maxima (β), lattice pressure (ε) and crystallite length (D) are as fellow

$$\beta\text{Cos}\theta = \frac{k\lambda}{D} + 4\varepsilon\text{Sin}\theta$$

Where λ is the wavelength of x-ray diffraction, k is constant and its value equal to

0.94 and θ is the diffraction peaks position. The βCosθ is plotted against 4Sinθ, and after linear fitting, the slope gives the value of lattice strain (ε) and inverse of intercept gives the value of crystallite size (D). The W-H plots of BFO nanomaterial synthesized by co-precipitations method are clearly shown in Figure
3.2 (a-d). The lattice strain calculated from W-H plot and found to be 0.0061,

e-ISSN 2320 –7876 www.ijfans.org
Vol.11, Iss.9, Dec 2022

0.0048, 0.0034 and 0.0021 at various sintering temperature from 400 to 300 ^{0}C respectively. This indicates that the lattice strains decreases with increasing sintering temperature.

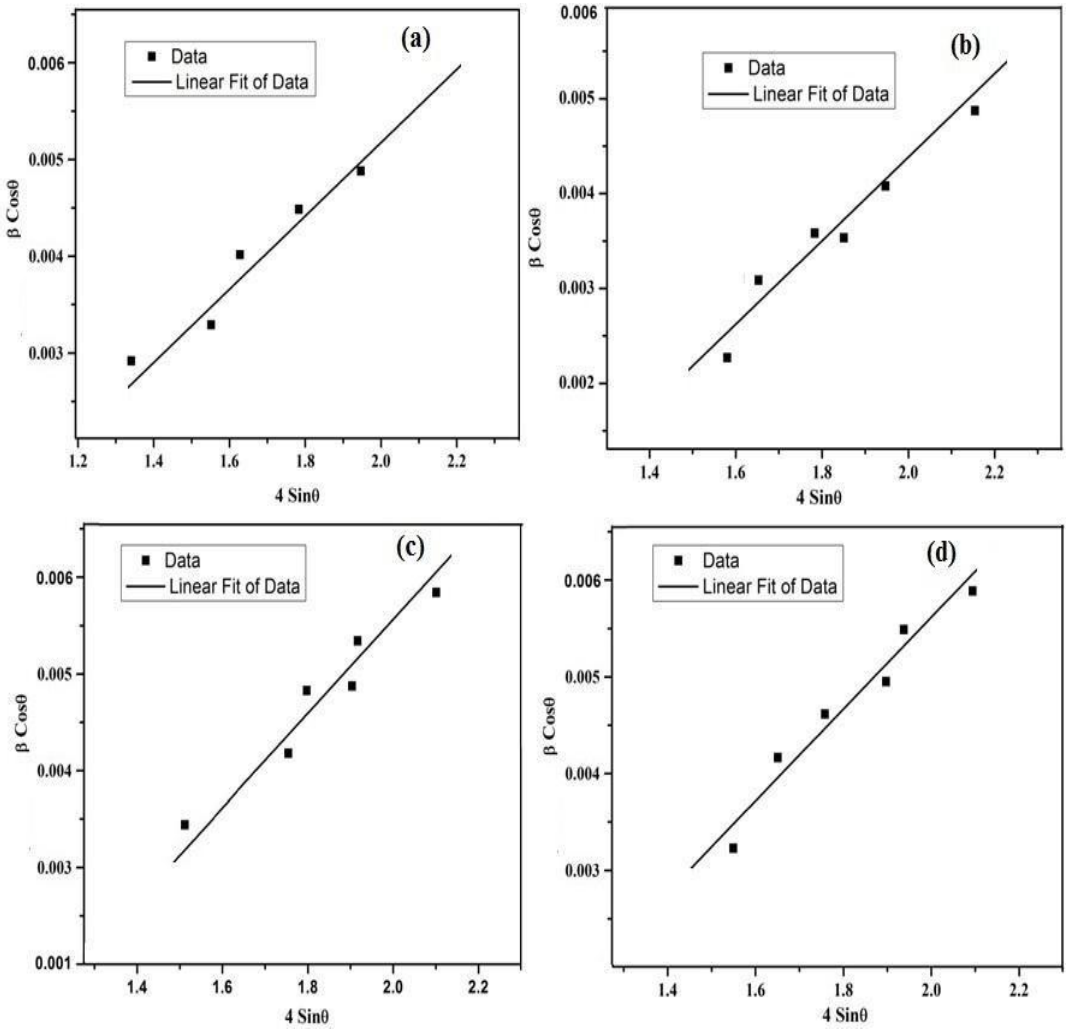

Figure 3.2 Williamson-Hall plots of BFO sintered at 400 ^{0}C to 300 ^{0}C.

e-ISSN 2320 –7876 www.ijfans.org
Vol.11, Iss.9, Dec 2022

Research Paper

3.3.3 Raman analysis

To in addition study the structural residences of BFO bulk material are employed the Raman spectroscopy measurements at room temperature. The Raman spectra of BFO bulk fabric sintered from 400 0C to 300 0C are recorded in the frequency range of a hundred-800 cm-1 are shown in parent three.3. There are thirteen Raman active modes consisting of four longitudinal optical A1 (LO) and nine transverse optical E (TO) phonons for rhombohedral R3c shape of pure BFO at room temperature (300 ok) as reported by using organization concept. The A1 (LO) and E (TO) modes are in particular originated in Raman spectra due to the vibration of Bi-O and Fe–O bond nicely correlated with institution concept. consistent with institution principle, predicts thirteen (4A1+9E) optical Raman energetic modes of BFO bulk with the rhombohedral crystal shape. in the gift investigation seven Raman lively modes inclusive of two A1 (a hundred and forty, 182 cm-1) and five E (264, 320, 430, 525, 613 cm-1) in the frequency range a hundred-1200 cm-1are located in the bulk fabric, which affirm the rhombohedral crystal structure

. Furthermore increase the sintering temperature from 400 ^{0}C to 300 ^{0}C the Raman active modes ($2A_1$+5E) such as 141, 182, 263, 322, 433, 526,

618 cm^{-1} 142, 184, 265, 323, 432, 528, 620 cm^{-1} and 143, 185, 266, 325, 431, 523,

624 cm^{-1} are frequently observed at room temperature.

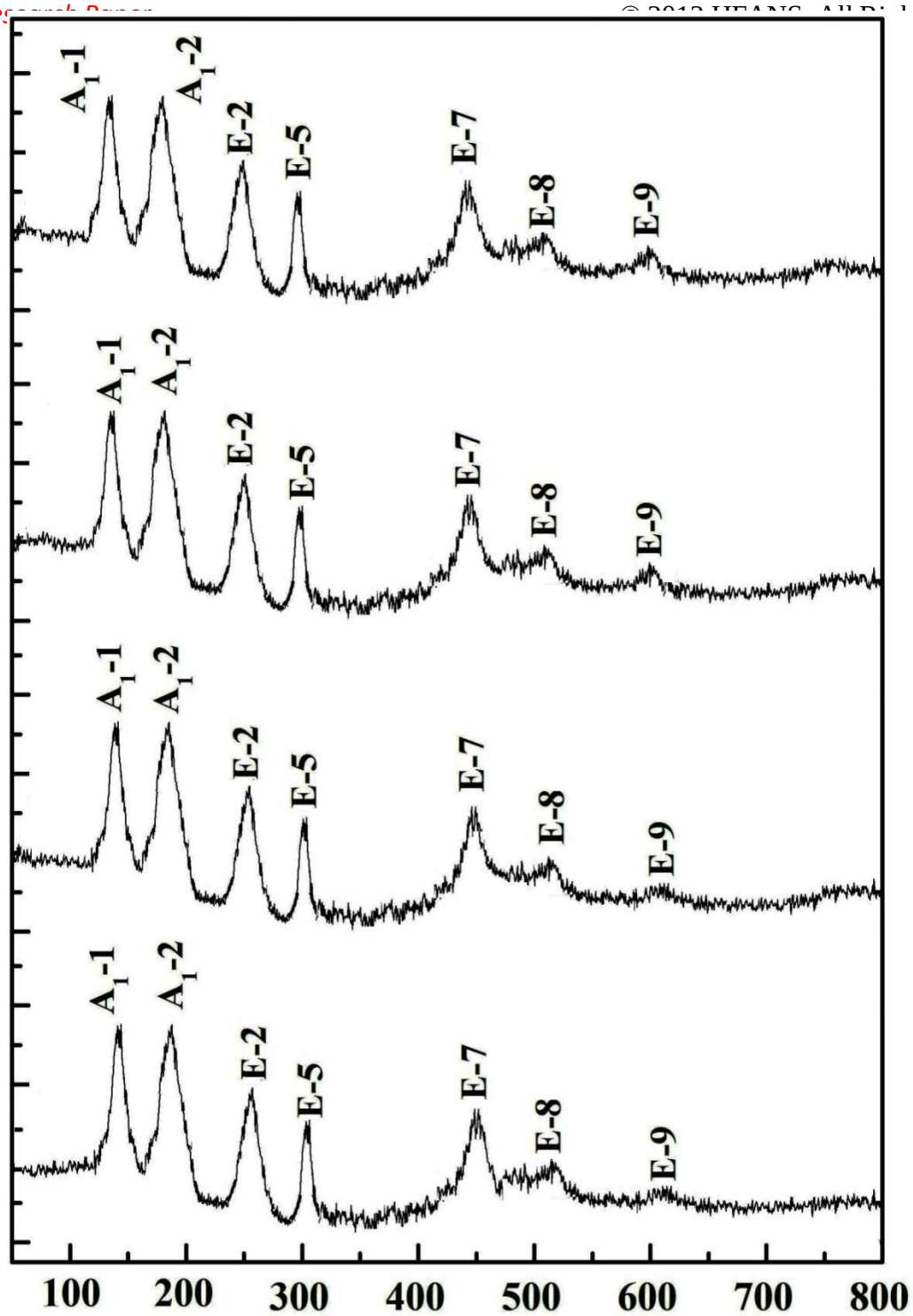

Figure 3.3 Raman spectra of BFO sintered at 400 ^{0}C to 300 ^{0}C.

The shifting of Raman active modes slightly higher frequency side may causes of structural misrepresentation, alteration in the bond lengths and bond angles of BFO as the shaking of FeO_6 octahedra are related with high-frequency modes. It is observed that increase the sintering temperature from 400 ^{0}C to 300 ^{0}C two Raman active modes of A_1(LO) and five modes of E(TO) attribute to rhombohedral crystal structure. Therefore, it may be concluded that there is no structural phase transformation well consistent with XRD result.

Transmission electron microscopy analysis

The microstructural characteristics of the BFO bulk material sintered at 500 ^{0}C were explored by employing transmission electron microscopy (TEM) in both the imaging and diffraction modes. Figures 3.4(a) and 3.4(b) show the image and selected area electron diffraction (SAED) pattern of BFO pellet respectively. The analysis of TEM micrograph and SAED pattern of BFO bulk have been studied using IMAGE J Software. TEM image of the BFO pellet show the presence of inter-connected nanoparticles (~25 nm) with high degree of crystallinity. The SAED pattern shows bright and sharp diffraction spots in the form of rings. This confirms the formation of crystalline nanoparticles. The calculated d-spacing ofthe various nano-rings in SAED pattern corresponds to (012), (110), (202) and
(024) planes of rhombohedral phase with R3c space group.

Surface topographic analysis

Scanning electron microscopy analysis

The surface morphology of the BFO polycrystalline material is examined by the field emission scanning electron microscopy (FESEM) technique sintered at various temperatures from 400 ^{0}C to 300 ^{0}C shown in Figure 3.5(a-d). The FESEM images of BFO material sintered at 400 ^{0}C revealed the diffused uniform micro-grains are closely packed and few pores/voids among the grains. Further increase the sintering temperature from 400 ^{0}C to 600 ^{0}C marigold like nanostructure appears throughout the surface. Moreover increases the sintering temperature

from 500 ^{0}C to 600 ^{0}C influenced the growth of crystallographic orientation leading to formed marigold flower like well cleared morphology. On the other hand, the BFO sintered at 300 ^{0}C is found to be agglomerated with irregular morphology throughout the surface. The average particle size increases from ~150 nm to 250 nm, with increasing the sintering temperature which indicatethat improves the density of nanomaterial

Atomic force microscopy analysis

The surface topographic studies of $BiFeO_3$ material have been carried out by atomic force microscopy (AFM) technique. It is clearly found that the surface topography dependence on the sintering temperature. It is clear from the AFM images the BFO pellet sintered at 400 ^{0}C has diffused spherical morphology with size of ~150 nm. Moreover, BFO sintered at 500 ^{0}C shows marigold flower like topographic image shown in Figure 3.6. With increase the sintering temperature from 500 ^{0}C to 600 ^{0}C well cleared marigold like nanostructure appeared throughout the surface. We are the foremost in reporting the marigold flower shaped morphology of BFO synthesized by co-precipitations methods. Moreover, the BFO sintered at 300 ^{0}C is found to be agglomerated primary small grains have high surface free energy and they tend to agglomerate faster and create irregular like (cylindrical and ellipsoidal) morphology. The grain size of BFO nanomaterialsintered from 400 ^{0}C to 300 ^{0}C temperatures is found to be ~100-200 nm. The root mean square (RMS) roughness and average roughness of each BFO pallet was measured by WSxM software. The RMS and average roughness is observed and found to be 12.42, 10.64, 3.43, 3.34 nm and 9.25, 3.26, 3.85, 1.15 nm respectively. RMS and average roughness decreases with increasing the sintering temperature from 400 ^{0}C to 300 ^{0}C, clearly indicates that increases the uniformity and smoothness of the surfaces.

e-ISSN 2320 –7876 www.ijfans.org
Vol.11, Iss.9, Dec 2022

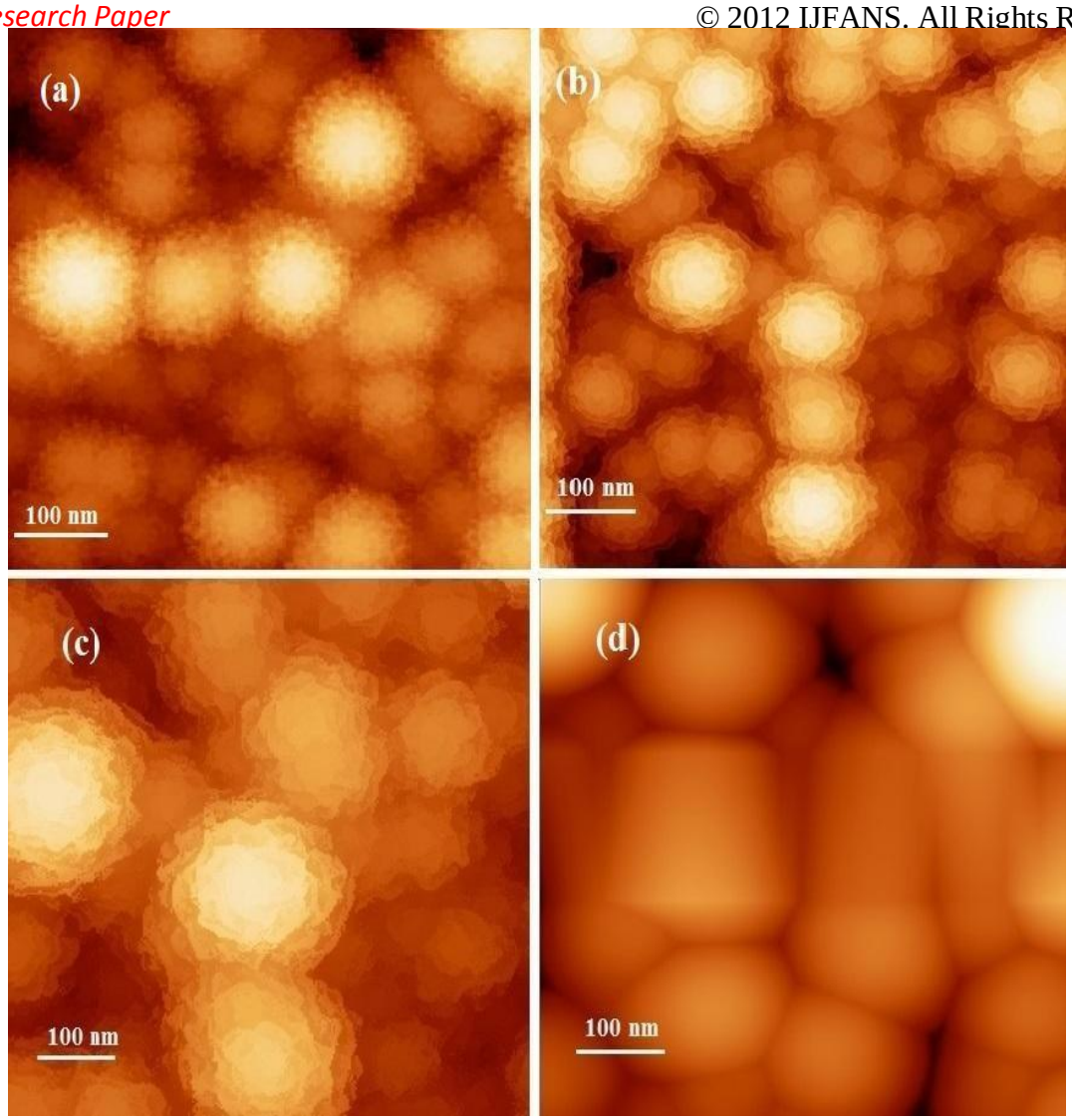

Figure 3.6 AFM topographic image of BFO sintered (a) 400 ^{0}C (b) 500 ^{0}C(c) 600 ^{0}C (d) 300 ^{0} C.

Dielectric analysis

The value of dielectric constant (ε') and Tan loss (δ) of BFO bulk material sintered at different temperature from 400 ^{0}C to 300 ^{0}C have been found to be 68, 109, 100, 93 and 0.14, 0.26, 0.21, 0.23respectively.

e-ISSN 2320 –7876 www.ijfans.org
Vol.11, Iss.9, Dec 2022

Research Paper

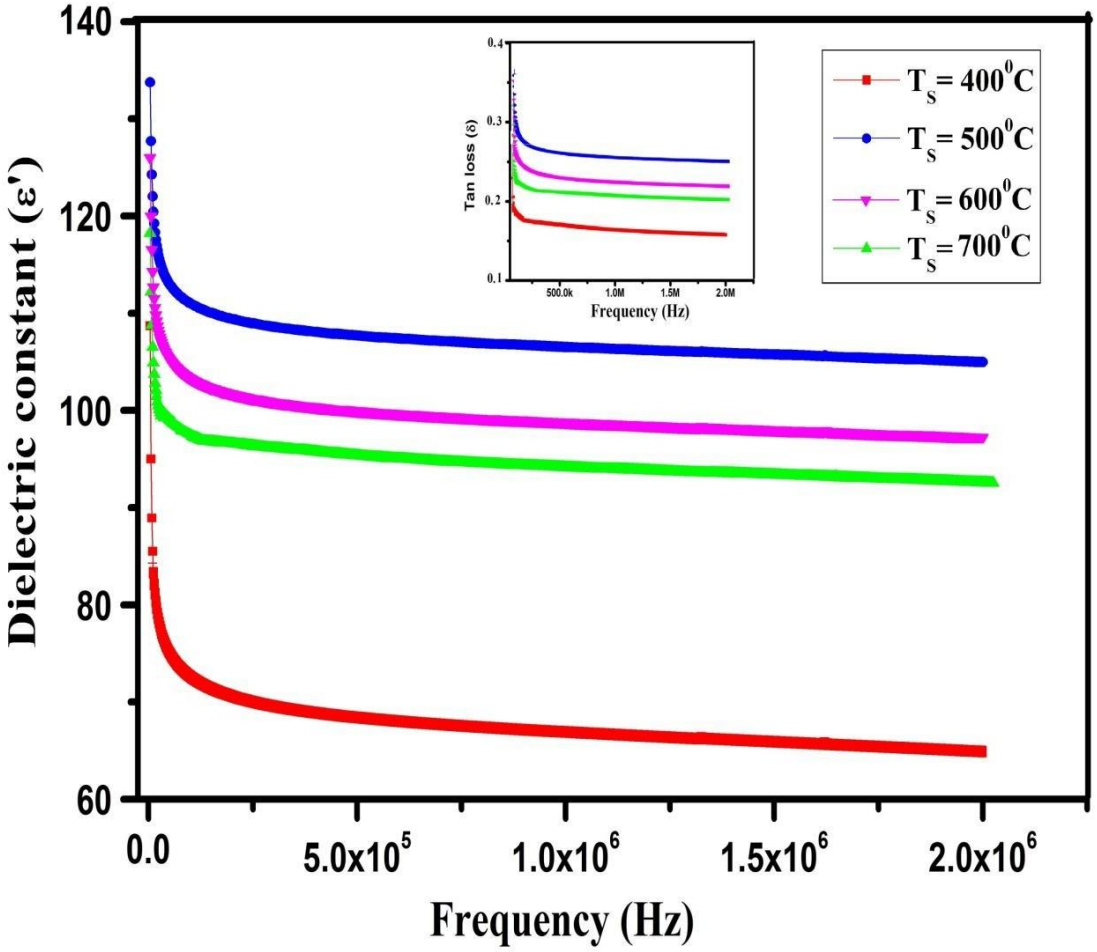

Figure 3.3 Dielectric constant of BFO sintered from 400 ^{0}C to 300 ^{0}C and inset shows tan loss as a function of frequency.

It is also observed that in lower frequency region, dielectric constant (ε') increases from 68 to 109 with increasing sintering temperature from 400 ^{0}C to 500 °C, it may be due to the increasing the density and corresponding to decrease the porosity of material. Further increase the sintering temperatures from 500 °C to 300 °C see from Figure 3.3 that the grain boundaries exhibit the tendency to blur,

leading to the sharp decrease in dielectric constant. The decrease in tan loss (δ) with increasing sintering temperature depends on stoichiometry, oxygen vacancies and composition of BFO material.

Conclusion

Co-precipitations technique has been used for the preparations of BFO nanomaterial. XRD pattern confirmed the rhombohedral crystal structure with space group R3c symmetry. Raman spectra also exhibits rhombohedral crystal structure sintered at various temperature from 400 ^{0}C to 300 ^{0}C. FESEM/AFM images showed marigold flower like surface structure of nanoparticles. It is also observed that fascinating marigold flower shaped morphology with increase the sintering temperature from 500 ^{0}C to 600 ^{0}C may be due to anisotropic oriented growth of nanoparticles. Moreover improved the magnetic property BFO sintered at 500 ^{0}C may be due to the oxygen vacancy or point defects in the material. The higher value of dielectric constant (ε') was found to be 109 sintered at 500 ^{0}C. However, increase the sintering temperature from 500 ^{0}C to 300 ^{0}C decrement in dielectric constant was observed may be due to leakage of current. The high value of dielectric constant and weak ferromagnetism in BFO sintered at 500 ^{0}C make these material useful for high density memory devices and potentials applications.

References

[1] K.J. Choi, M. Biegalski, Y. Li, A. Sharan, J. Schubert, R. Uecker, P. Reiche, Y. Chen, X. Pan, V. Gopalan, Enhancement of ferroelectricity in strained $BaTiO_3$ thin films, Science, 306, (2004), 1005-1009.

[2] M. Dawber, K. M. Rabe, and J. F. Scott, Physics of thin-film ferroelectric oxides, Rev. Mod. Phys. 77, (2005), 1083.

[3] G. Gerra, A. K. Tagantsev, N, Setter, K. parlinski, Ionic Polarizability of Conductive Metal Oxides and Critical Thickness for Ferroelectricity in $BaTiO_3$ Phys. Rev. Lett. 96, (2006), 107603.

[4] H. Obara, A. Yamamoto, C.-H. Lee, K. Kobayashi, A. Matsumoto, R. Funahashi, Thermoelectric properties of Y-doped polycrystalline $SrTiO_3$, Japanese journal of applied

physics, 43, (2004), 540.

[5] W.H. Chan, Z. Xu, J. Zhai, H. Chen, Uncooled tunable pyroelectric response of anti-ferroelectric $Pb_{0.97}La_{0.02}(Zr_{0.65}Sn_{0.22}Ti_{0.13})O_3$ perovskite, Applied Physics Letters, 87, (2005), 192904.

[6] G. Arlt, D. Hennings, Dielectric properties of fine-grained barium titanate ceramics, Journal of applied physics, 58, (1985), 1619-1625.

[7] O. Bohnke, C. Bohnke, J. Fourquet, Mechanism of ionic conduction and electrochemical intercalation of lithium into the perovskite lanthanum lithium titanate, Solid State Ionics, 91 (1996) 21-31.

[8] M. Kamalasanan, S. Chandra, P. Joshi, A. Mansingh, Structural and optical properties of sol-gel-processed $BaTiO_3$ ferroelectric thin films, Applied physics letters, 59, (1991), 3547-3549.

[9] P. G. Radaelli, G. Iannone, M. Marezio, H. Y. Hwang, S-W. Cheong, J. D. Jorgensen, D. N. Argyriou, Phys. Rev. B 56, (1997), 8265.

[10] Y. Tomioka, A. Asamitsu, Y. Moritomo, H. Kuwahara, Y. Tokura, Phys. Rev. Lett. 74, (1995), 5108.

[11] F.C. Zhang and T. M. Rice, Effective Hamiltonian for the superconducting Cu oxides, Phys. Rev. B 37, (1988), 3759(R).

[12] Y. Tokura, H. Takagi and S. Uchida, A superconducting copper oxide compound with electrons as the charge carriers, Nature 337, (1989), 345-347.

[13] A. Kingon, S. Streiffer, C. Basceri, S. Summerfelt, High-permittivity perovskite thin films for dynamic random-access memories, MRS Bulletin, 21, (1996), 46- 52.

[14] E. Nenasheva, A. Kanareykin, N. Kartenko, A. Dedyk, S. Karmanenko, Ceramicsmaterial based on (Ba, Sr)TiO_3 solid solutions for tunable microwave devices, Journal of Electroceramics, 13, (2004), 235-238.

[15] D. Dimos, C. Mueller, Perovskite Thin Films for High-Frequency Capacitor Applications 1, Annual Review of Material Science, 28, (1998), 397- 419.

[16] L. Protesescu, S. Yakunin, M.I. Bodnarchuk, F. Krieg, R. Caputo, C.H. Hendon,

R.X. Yang, A. Walsh, M.V. Kovalenko, Nanocrystals of cesium lead halide perovskites ($CsPbX_3$, X= Cl, Br, and I): novel optoelectronic material showing bright emission with wide color gamut, Nano letters, 15, (2015), 3692-3696.

[17] K. Uchino, S. Nomura, L.E. Cross, R.E. Newnham, S.J. Jang, Electrostrictive effect in perovskites and its transducer applications, Journal of Material Science 16, (1981), 569-578.

[18] H. Obayashi, Y. Sakurai, T. Gejo, Perovskite-type oxides as ethanol sensors, Journal of Solid State Chemistry 17, (1976), 299-303.

[19] P. Muralt, R. Polcawich, S. T.-M. Kinstry, Piezoelectric thin films for sensors, actuators, and energy harvesting, MRS bulletin, 34, (2009), 658-664.

[20] M.T. Sebastian, Dielectric material for wireless communication, Elsevier, 2010.

[21] D. Sando, A. Agbelele, D. Rahmedov, J. Liu, P. Rovillain, C. Toulouse, I. C. Infante, A. P. Pyatakov, S. Fusil, E. Jacquet, C. Carrétéro, C. Deranlot, S. Lisenkov, D. Wang, J-M. Le Breton, M. Cazayous, A. Sacuto, J. Juraszek, A. K. Zvezdin, L. Bellaiche, B. Dkhil, A. Barthélémy & M. Bibes, Crafting the magnonic and spintronic response of $BiFeO_3$ films by epitaxial strain, Nature Material, 12, (2013), 641-646.

[22] J. X. Zhang, Q. He, M. Trassin, W. Luo, D. Yi, M. D. Rossell, P. Yu, L. You, C. H. Wang, C. Y. Kuo, J.T. Heron, Z. Hu, R. J. Zeches, H. J. Lin, A. Tanaka, C. T.Chen, L. H. Tjeng, Y.-H. Chu, and R. Ramesh, Microscopic origin of the giant ferroelectric polarization in tetragonal like $BiFeO_3$, Phys. Rev. Lett. 107, (2011), 147602.

[23] S. Gnewuch, E. E. Rodriguez, The fourth ferroic order: current status onferrotoroidic material, Journal of Solid State Chemistry, 271, (2019), 175-190.

[24] G. A. Smolenskii, I.E. Chupis, Ferroelectromagnets, Sov. Phys. Usp. 25, (1982),475.

[25] J.C. Maxwell, On physical lines of force, Philosophical Magazine 1861.

[26] Z. Wang, Y. Zhang, Y. Wang, Y. Li, H. Luo, J. Li, D. Viehland, Magnetoelectric assisted 180° magnetization switching for electric field addressable writing in magnetoresistive random-access memory, ACS Nano, 8(8), (2014), 7793-7800.

[27] J. K. Kim, S. S. Kim, W-J Kim, Sol–gel synthesis and properties of multiferroic $BiFeO_3$, Material Letters, 59, (2005), 29-30.